JACS
JOURNAL OF THE AMERICAN CHEMICAL SOCIETY

Article

pubs.acs.org/JACS

Reverse Water–Gas Shift or Sabatier Methanation on Ni(110)? Stable Surface Species at Near-Ambient Pressure

Matteo Roiaz,[†,§] Enrico Monachino,[†,∥] Carlo Dri,[†,‡] Mark Greiner,[⊥] Axel Knop-Gericke,[⊥] Robert Schlögl,[⊥] Giovanni Comelli,[†,‡] and Erik Vesselli*[,†,‡]

[†]Physics Department, University of Trieste, via Valerio 2, I-34127 Trieste, Italy

[‡]IOM-CNR Laboratorio TASC, Area Science Park, S.S. 14 km 163.5, I-34149 Basovizza (Trieste), Italy

[⊥]Abteilung Anorganische Chemie, Fritz-Haber Institut der Max-Planck Gesellschaft, Faradayweg 4-6, 14195 Berlin, Germany

Supporting Information

ABSTRACT: The interaction of CO, CO_2, CO + H_2, CO_2 + H_2, and CO + CO_2 + H_2 with the nickel (110) single crystal termination has been investigated at 10^{-1} mbar in situ as a function of the surface temperature in the 300–525 K range by means of infrared-visible sum frequency generation (IR–vis SFG) vibrational spectroscopy and by near-ambient pressure X-ray photoelectron spectroscopy (NAP-XPS). Several stable surface species have been observed and identified. Besides atomic carbon and precursors for graphenic C phases, five nonequivalent CO species have been distinguished, evidencing the role of coadsorption effects with H and C atoms, of H-induced activation of CO, and of surface reconstruction. At low temperature, carbonate species produced by the interaction of CO_2 with atomic oxygen, which stems from the dissociation of CO_2 into CO + O, are found on the surface. A metastable activated CO_2^- species is also detected, being at the same time a precursor state toward dissociation into CO and O in the reverse water–gas shift mechanism and a reactive species that undergoes direct conversion in the Sabatier methanation process. Finally, the stability of ethylidyne is deduced on the basis of our spectroscopic observations.

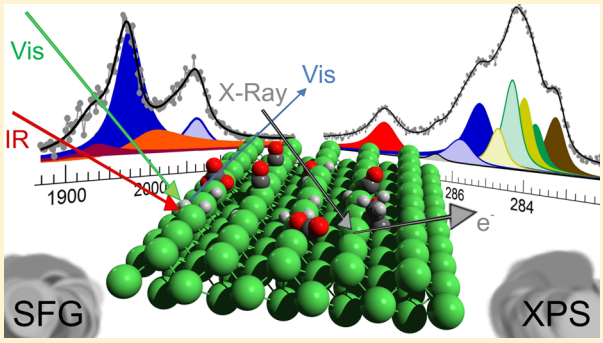

INTRODUCTION

At present, the practical conversion of CO_2 in industrial processes is still limited to few cases like the synthesis of urea, salicylic acid, and polycarbonates for plastics. However, the catalytic hydrogenation of carbon dioxide is currently attracting growing attention for the clean synthesis of energy vectors and chemicals.[1,2] In addition to the well-known sequestration issues related to its greenhouse effects, CO_2 is expected to be a nearly zero or even negative cost feedstock for conversion into fuels.[1] In this perspective, many research efforts are being dedicated to better understand its (electro)catalytic conversion mechanisms. More specifically, a large variety of processes to obtain methane and higher hydrocarbons, methanol and higher alcohols, formic acid and other oxygenates are currently under investigation.[3] Generally speaking, and depending on the catalyst and on the specific reaction conditions, hydrogenation of CO_2 can produce CO via the reverse water–gas shift reaction (RWGS: $CO_2 + H_2 \rightarrow CO + H_2O$) or methane via the methanation process ($CO_2 + 4H_2 \rightarrow CH_4 + 2H_2O$). In principle the RWGS reaction could represent an intermediate step in the methanation process, being possibly followed by the methanation of CO. In this respect, an extended set of model investigations has appeared in the scientific literature, with the aim of shedding light on the atomic-level details of the underlying reaction mechanisms. In particular, nickel was reported to play an important role as a catalyst or as a dopant since the early studies of the Sabatier process.[1−9] However, there is still a consistent gap between the applicable reaction conditions of industrial supported heterogeneous catalysts and both theoretical and experimental modeling conditions. This is mainly ascribed to the well-known issues related to the material and pressure gaps. In relation to nickel single crystal surfaces, very detailed investigations concerning the CO_2 and CO hydrogenation mechanisms have been reported, suggesting the presence of an activated CO_2^- species that can both dissociate into CO + O or undergo direct hydrogenation to a stable formate species or via a reactive hydrocarboxyl intermediate.[8,10−19] Recently, deeper insight has been obtained on Ni(110) by exploiting near-ambient pressure X-ray photoelectron (NAP-XPS) spectroscopy measurements performed in situ in the 10^{-1} mbar range,[11] thus clarifying the role of metallic, oxidic, and carbidic/graphenic states of the surface.

Here we report the results obtained by coupling NAP-XPS with the complementary approach of infrared-visible sum-frequency generation (IR–vis SFG) vibrational spectroscopy.

Received: December 22, 2015
Published: March 8, 2016

DOI: 10.1021/jacs.5b13366
J. Am. Chem. Soc. 2016, 138, 4146–4154

The latter technique is indeed intrinsically sensitive to interfaces and allows bridging the pressure gap issues,[20,21] thus providing insight onto the catalyst's surface during the reaction with the gas phase, and even in liquid and under electrocatalytic conditions. By combining NAP-XPS and IR−vis SFG approaches, and by comparing the corresponding spectroscopic results with previous literature data, we are able to identify the presence of several stable species on the Ni(110) surface during the reaction of CO_2 and CO with hydrogen in the 300−525 K range. Besides atomic carbon and precursors for graphenic phases, five distinct CO species, an activated CO_2^- reaction precursor, carbonate, and the fingerprints of a stable ethylidyne intermediate are observed.

METHODS

SFG Experiments. Infrared-visible sum frequency generation[22] vibrational spectroscopy measurements were performed at the Physics Department of the University of Trieste in a dedicated setup described elsewhere.[23] The Ni(110) sample was mounted by means of Ta wires that allowed resistive heating up to 1300 K in ultrahigh vacuum (UHV) and up to 800 K in the reactor (K-type thermocouple). The system allows transferring the sample between the high-pressure cell and the UHV environment without breaking the vacuum. The reactor was equipped with a gas handling system in order to control the pressure of the reactants, allowing for constant-flow steady-state reaction conditions, while the inlet of the infrared and visible beams, as well as the outlet of the SFG signal, were provided by UHV-compatible BaF_2 windows. The excitation source and the detection system (EKSPLA) deliver a 532 nm visible beam and tunable IR radiation in the 1000−4500 cm^{-1} range, and yield an ultimate energy resolution of the SFG signal better than 6 cm^{-1}. In the present study all spectra were collected in the p−p−p polarization configuration (SFG-visible-infrared).

For each experiment, the Ni(110) surface was cleaned by standard cycles of Ar^+ sputtering and annealing in UHV. Surface order was checked by LEED, yielding a sharp (1 × 1) pattern with extremely low background. Typical spectra acquisition time was about 15 min for the C−O and about 180 min for the C−H stretching regions, respectively. Data were collected, as for the XPS spectra, under steady-state conditions at equilibrium, since time-resolution was not enough to gather information about transients. The sample was reprepared after each experiment.

After normalization to the impinging visible and IR intensities, SFG spectra were analyzed by least-squares fitting methods to the following widely used parametric, effective expression of the nonlinear second order susceptibility,[24−27] explicitly accounting for the IR resonances of the IR−vis transitions and for the nonresonant background:

$$\frac{I_{SFG}(\omega_{IR})}{I_{vis}I_{IR}(\omega_{IR})} \sim \left| A_{NRes} + \sum_k \frac{A_k e^{i\Delta\varphi_k}}{\omega_{IR} - \omega_k + i\Gamma_k} \right|^2$$

In this expression A_{NRes} and A_k account for the real amplitudes of the nonresonant and kth-resonant contributions, respectively, $\Delta\varphi_k$ is the phase difference between the kth-resonance and the nonresonant background, ω_k is the energy of the kth-resonance, and Γ_k its Lorentzian broadening related to the resonance lifetime. Additional details about the SFG experimental setup, the data analysis and the interpretation of the spectral quantities plotted in the figures can be found in a previous contribution.[23]

A very detailed and careful analysis of the SFG spectra was performed in order to obtain a reliable identification of the contributions originating from different species in the C−O stretching region, particularly for the S_{1-3} features associated with bridge and on-top CO in coadsorption phases (Table 1). A unique set of "best" line shape parameters was obtained recursively, allowing optimal fitting of the whole data set, apart from slight variations in the line positions and/or changes in the resonance phase values. In preliminary experiments, lineshapes for the on-top and bridge carbon monoxide species were independently derived from the spectra in which each single species was separately present, as obtained by pure CO or pure CO_2 adsorption under UHV conditions from a 10^{-7} mbar background. For each SFG spectrum throughout the manuscript we plot the normalized SFG signal (dots) together with the best fit (black lines) according to the above function that accounts for all the interference cross terms. In addition, we also plot (color-filled curves) the intensity of each kth resonant contribution and its interference with the nonresonant background, thus representing the deconvoluted intensity modulations with respect to the nonresonant background, according to the following function:

$$I_{SFG,k}(\omega_{IR}) \sim \left| A_{NRes} + \frac{A_k e^{i\Delta\varphi_k}}{\omega_{IR} - \omega_k + i\Gamma_k} \right|^2$$

Further details about the plots of the SFG data deconvolution can be found in our previous work.[23]

Table 1. Energies of the Observed Vibrational Modes, Comparison with the Literature, and Proposed Identification of the Stable Species[a]

this work			reference	
value/range	mode	species	value/range	system
1927−1936	C−O str.	CO[b] bridge (S_1)	1874−1940[45,46]	CO + H + C/Ni(110)
1959−1988	C−O str.	CO bridge	1840−1980[31,32]	Ni(110)
1996−2007	C−O str.	CO[b] on-top (S_2)	2000−2070[45,46]	CO + H + C/Ni(110)
2018−2035	C−O str.	CO[b] on-top (S_3)	2000−2070[45,46]	CO + H + C/Ni(110)
2061−2088	C−O str.	CO on-top	2000−2090[31,32]	Ni(110)
2850 ± 5	C−H (s) str.	CCH_3− ethylidyne	2883[51]	Ni(111)
2935 ± 5	C−H (as) str.	CCH_3− ethylidyne	2940[51]	Ni(111)

[a]All values in cm^{-1} [b]Coadsorbed with other intermediates, observed under reduction conditions.

NAP-XPS Experiments. Near-ambient pressure (mbar range) X-ray photoelectron spectroscopy measurements were carried out at the ISISS end-station of the Bessy synchrotron radiation facility at the Helmholtz Zentrum Berlin (Germany).[28] The same Ni(110) single crystal used for the IR−vis SFG measurements was mounted on a sapphire holder by means of Ta supports and screws. Temperature was measured with a K-type thermocouple, and the sample was heated by laser irradiation of its unpolished back face. After each reactivity experiment, the Ni(110) surface was cleaned by standard cycles of ion sputtering and annealing in high vacuum. The flux and pressure of the gases introduced into the experimental chamber were handled by means of mass-flow controllers and a motorized valve. Gas purity was monitored using a quadrupole mass spectrometer. NAP-XPS spectra were collected in normal emission geometry and binding energies were calibrated with respect to the Fermi level. After normalization and subtraction of a Shirley background,[29] spectra were analyzed by least-squares fitting of the data with Doniach-Šunjić profiles,[30] convoluted with a Gaussian envelope to account for experimental resolution, inhomogeneity, and thermal broadening. A very detailed and careful analysis of the C 1s core level spectra was performed in order to obtain a unique and reliable identification of the contributions originating from different species. This was achieved by determining a single set of line shape parameters that allowed optimal fitting of all the C 1s spectra. Within this set, in order to reduce the number of degrees of freedom, identical lineshapes were used for groups of similar species (Lorentzian width and asymmetry) in the framework of a global fit procedure, in which the whole data set was considered. Selected line positions and Gaussian broadening profiles were let to vary in order to account for effects associated with local surface reconstruction and coadsorption depending on the chemical conditions, yielding small

DOI: 10.1021/jacs.5b13366
J. Am. Chem. Soc. 2016, 138, 4146−4154

core level shifts (±0.2 eV) and/or inhomogeneity broadening. The resulting binding energy values and/or intervals were assigned to chemical species on the basis of literature data as reported in the text.

RESULTS AND DISCUSSION

Benchmark exposure of the Ni(110) surface to carbon monoxide at 10^{-2} mbar in the 300−425 K range yields two features in the C−O stretching region of the SFG vibrational spectra (Figure 1), assigned to bridge (1982−1988 cm^{-1}, dark blue) and on-top (2073−2088 cm^{-1}, light blue) adsorption configurations, respectively, in agreement with both previous literature,[31,32] and core level photoemission data. The C 1*s* spectra, (Figure 2, panel b) measured at 425 K in 10^{-1} mbar CO, show indeed contributions at 285.4 and 285.8 eV, attributed to bridge and terminal CO,[33] respectively, while the remaining three peaks at lower binding energy are associated with surface or interstitial atomic carbon and graphene domains as we shall see in the following. Interestingly, in the SFG spectra a screening of the signal is observed between 350 and 375 K, in analogy to CO adsorption on Ni(111),[34] yielding a decrease in the intensities. The phenomenon is related to changes in the electronic part of the SFG process, i.e., in a modification of the Raman tensor due to coverage effects. In this temperature range, a CO-induced (111) reconstruction of Ni(110) is expected at NAP conditions,[11,35] thus explaining the observed similarities with the behavior of Ni(111). Heating to 425 K promotes carbon monoxide decomposition (Figure 2, panel b), starting from surface defective sites,[7] to form carbon deposits (283.2−283.5 eV, depending on the reaction conditions, brown), and strongly (284.5−285.0 eV, light yellow) and weakly interacting (284.0−284.3 eV, yellow) graphene seeding domains.[11,36] The C 1*s* line position of the above species was found to vary within the indicated intervals, depending on the chemical environment, due to coadsorption and reconstruction effects. Indeed, the line position associated with atomic carbon can shift accordingly as already reported in the literature and is also related to surface-bulk dissolution processes.[37] At the low reaction temperatures adopted in this work, the latter mechanisms are expected to be in competition with the formation of graphene flakes. Graphene extensive growth is expected to occur only at higher temperature (above 700 K) on the basis of previous studies where, however, thermal cracking of hydrocarbons or bulk carbides were exploited as carbon sources.[37,38] In our case, a near-ambient pressure gas phase of coreactants like hydrogen and carbon oxides is present, yielding a higher surface mobility of the metal atoms and thus allowing for extensive surface reconstruction processes already at 400 K as previously observed by in situ X-ray diffraction techniques.[35] Therefore, the growth of both weakly and strongly interacting graphene seeding flakes already at 425 K is plausible. The finite size of the graphenic domains yielding intercalation of chemical species like carbon monoxide at near-ambient pressure conditions may finally account for the observed C 1*s* chemical shifts.[39−41] A summary of the vibrational energies and core level binding energies of the stable species identified in the present work is reported in Tables 1 and 2, respectively, together with the assignment proposed on the basis of literature data. Further heating above 425 K (not shown) in a CO environment leads to the progressive accumulation of carbon, yielding graphene growth, up to complete surface passivation.[11]

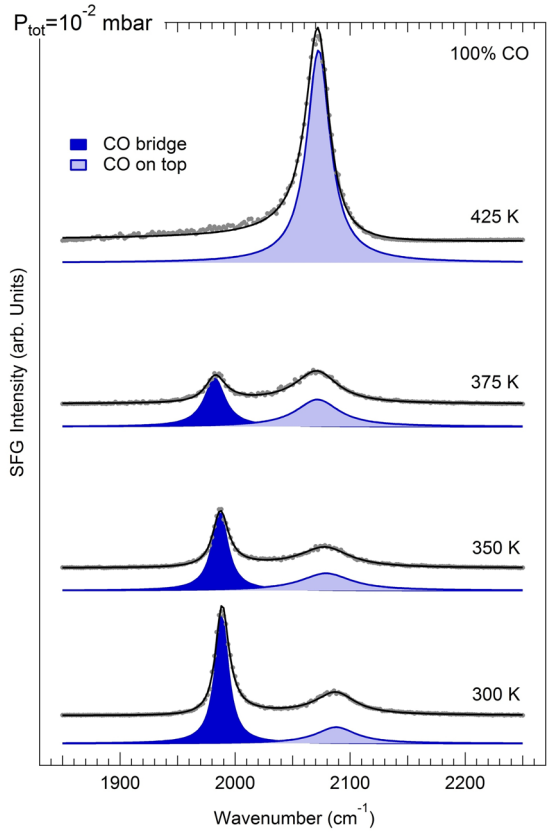

Figure 1. IR−vis SFG intensity spectra in the C−O stretching region collected in situ upon exposure of the clean Ni(110) surface to 10^{-2} mbar CO at selected temperature steps, increasing from bottom to top; data (gray dots) and the results of the least-squares fitting (black curves) are shown; color-filled curves represent deconvoluted intensity modulations with respect to the nonresonant background. [λ_{vis} = 532 nm; p−p−p polarization].

Exposure of Ni(110) to 10^{-2} mbar of CO_2 yields dissociation of the molecule into CO and O fragments and a lower CO coverage with respect to the previous case (Figure 2, panel d vs panel b, blue peaks). Atomic oxygen accumulates at the surface yielding progressive oxidation and passivation of the metal (see Supporting Information). This is in agreement with previous observations reporting that, under reaction conditions, a careful balance of CO and CO_2 gas phase concentrations is needed to prevent carbonization and oxidation of the surface,[11] thereby preserving its metallic character, which is related to the conversion efficiency in the carbon dioxide reduction process. Removal of surface oxygen by CO is necessary for keeping the surface metallic (as surface oxygen removal is inefficient with H_2 due to the high activation barrier of the O + 2H → H_2O reaction).[42]

Coming back to the NAP-XPS, in addition to the fingerprints of CO and C phases, two other features can be observed in the C 1*s* spectra that were obtained during exposure of the Ni(110) surface to CO_2 at 10^{-2} mbar at 425 K (Figure 2, panel d). The first is the broad feature at 288.3−288.5 eV (red) that can be attributed to carbonate,[11,43,44] originating from the interaction of CO_2 with atomic oxygen species that stem from previous CO_2 dissociation. The second feature is a smaller peak at 286.6 eV (gray), which can be resolved with difficulty (see the Methods section for details about the data analysis procedure): this feature is more evident in the spectra collected under hydrogenation reaction conditions reported in the following. It

DOI: 10.1021/jacs.5b13366
J. Am. Chem. Soc. 2016, 138, 4146−4154

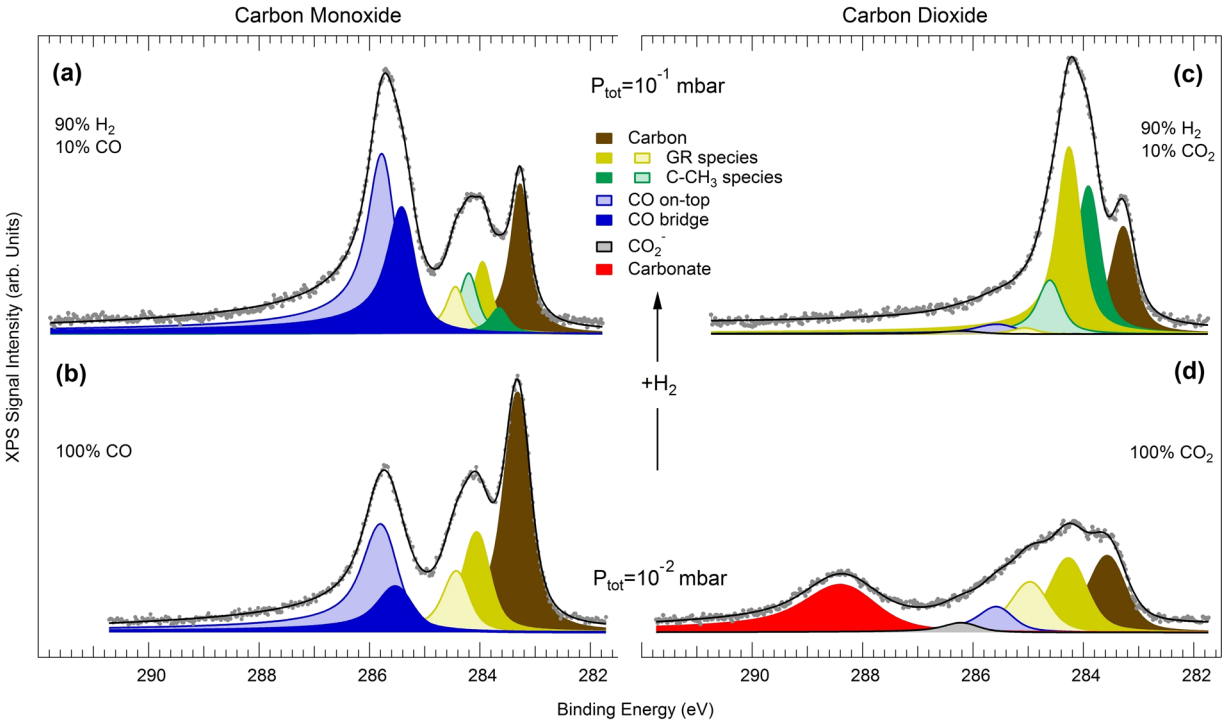

Figure 2. NAP-XPS C 1*s* core level spectra collected in situ upon exposure of the clean Ni(110) surface to CO (panel b) or to CO_2 (panel d) at 10^{-2} mbar, and under reduction conditions by adding H_2 (p_{H2}/p_{CO} = 9, panel a, and p_{H2}/p_{CO2} = 9, panel c, respectively) at 425 K and a total pressure of 10^{-1} mbar. The deconvolution (color) of the data (gray dots) obtained by means of least-squares fitting (black curves) is also shown. [$h\nu$ = 450 eV].

Table 2. C 1*s* Core Level Binding Energies, Comparison with the Literature, and Proposed Identification of the Stable Species[a]

this work		reference	
value/range	species	value/range	system
283.2–283.5	surface and dissolved carbon	283.2–283.8[11,36,37,47,57–59]	Ni(111), Ni(110), Ni
283.7–284.0	CCH_3–ethylidyne	283.95[47]	Pt(111)
284.0–284.3	graphene (weakly interacting)	284.0–284.4[11,36,37,47,57]	Ni(111), Ni(110), Ni
284.1–284.6	CCH_3–ethylidyne	284.32[47]	Pt(111)
284.5–285.0	graphene (strongly interacting)	284.5–284.8[11,36,37,47,57,58]	Ni(111), Ni(110), Ni
285.4–285.5	CO bridge	285.3[33]	Ni(111)
285.8	CO on-top	285.9[33]	Ni(111)
286.6	CO_2^-	286.2[12,13]	Ni(110)
288.3–288.5	CO_3^-–carbonate	288–289[11,43,44]	Fe(110), Ni(110)

[a]All values in eV.

is associated with the presence of activated, chemisorbed CO_2^- species at the Ni(110) surface, on the basis of previous studies of CO_2 adsorption investigated by means of a combination of XPS, high resolution electron energy loss spectroscopy, scanning tunneling microscopy, and density functional theory methods.[10,13,14] It has already been proven both experimentally and theoretically that this CO_2^- species on Ni(110) is both a precursor to dissociation into CO and O (RWGS mechanism) and a reactive state that undergoes fast conversion in the direct hydrogenation process (Sabatier methanation mechanism).[12,15] When adding hydrogen to the feedstock the two CO_2 conversion reactions are expected to proceed through parallel routes. Hydrogenation of CO is also effective, as we shall see in the following, and represents an alternative and parallel CO_2 methanation route that involves RWGS, sequentially followed by the methanation of CO. This interesting insight corroborates information on γ-alumina supported Ni catalysts.[3]

With the addition of hydrogen, accumulation of oxygen (i.e., from the CO_2 + H_2 reaction) or carbon (i.e., from the CO + H_2 reaction) still occurs, in analogy to the pure CO_2 and pure CO cases, respectively.[11] This is evident from the O 1*s* core level spectra (see Supporting Information). Proceeding in order and starting from the CO+H_2 case, the fingerprint of three additional contributions to the C–O stretching vibrational SFG spectra can be observed (Figure 3, left panel) in the 1927–1936 cm^{-1} (S_1, brown), 1996–2007 cm^{-1} (S_2, orange), and 2018–2035 cm^{-1} (S_3, pink) ranges. The S_1 feature is observed at low temperature also for the CO_2 + H_2 reaction (Figure 3, right panel). In this latter case, however, oxygen accumulates at the Ni(110) surface, thus passivating the surface as soon as the temperature is raised (see Supporting Information).[11] This happens due to the slow oxygen reduction by hydrogen at Ni,[42] and to the faster rate of oxygen production by the CO_2 reduction reaction that is promoted by hydrogen.[12,15] In parallel, two additional peaks appear in the C 1*s* core level spectra (Figure 2, panels a and c, light and dark green) in the 283.7–284.0 and 284.1–284.6 eV ranges.

DOI: 10.1021/jacs.5b13366
J. Am. Chem. Soc. 2016, 138, 4146–4154

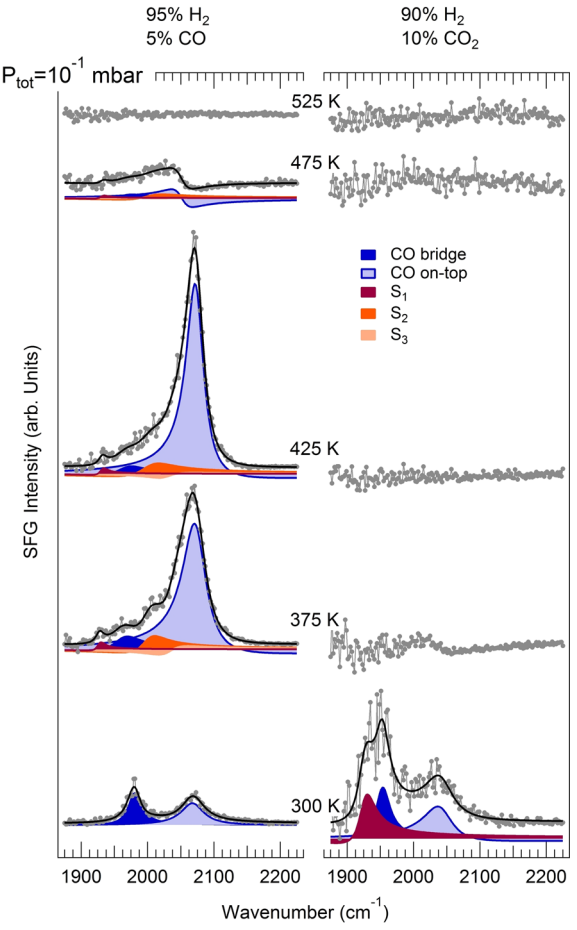

Figure 3. IR–vis SFG intensity spectra in the C–O stretching region collected in situ during the hydrogen reduction of CO (left panel), and of CO_2 (right panel) at a total pressure of 10^{-1} mbar on the Ni(110) surface for progressively increasing temperature (from bottom to top); data (gray dots) and the results of the least-squares fitting (black curves) are shown; color-filled curves represent deconvoluted intensity modulations with respect to the nonresonant background. [λ_{vis} = 532 nm; p–p–p polarization].

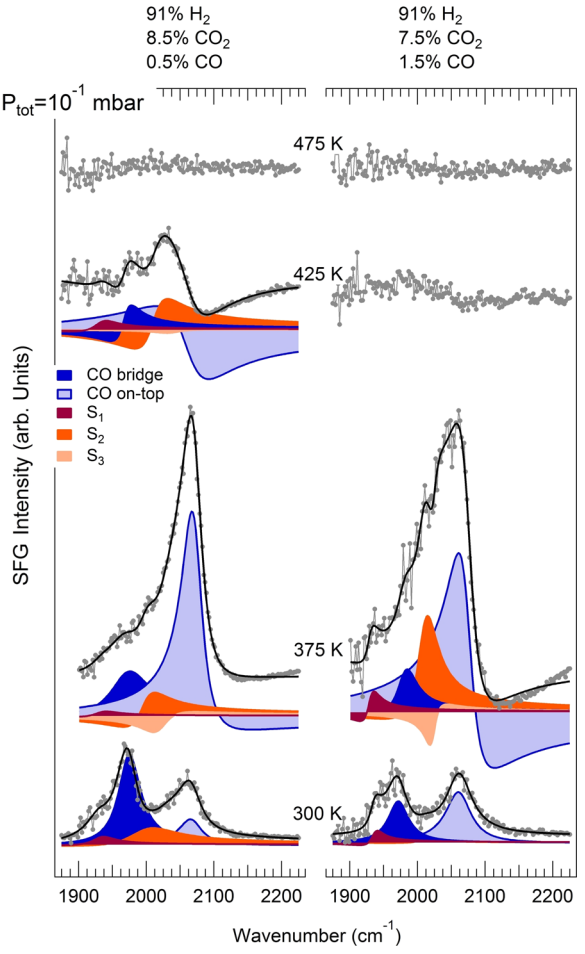

Figure 4. IR–vis SFG intensity spectra in the C–O stretching region collected in situ during the reaction of CO, CO_2 and H_2 at a total pressure of 10^{-1} mbar on the Ni(110) surface for progressively increasing temperature (from bottom to top); data sets corresponding to two different CO_2/CO pressure ratios are reported in the two panels (left and right); data (gray dots) and the results of the least-squares fitting (black curves) are shown; color-filled curves represent deconvoluted intensity modulations with respect to the nonresonant background. [λ_{vis} = 532 nm; p–p–p polarization].

The same spectral features appear also in the case where all three gases are introduced at the same time as feedstock (Figures 4 and 5). The phase relation of the SFG vibrational resonances with respect to the nonresonant background ($\Delta\varphi_k$) varies with temperature under reaction conditions (Figure 4) due to modifications of the local geometric and electronic structures of the system, yielding evident changes in the spectral line shape. Both carbonate and chemisorbed carbon dioxide species can be identified in the NAP-XPS spectra at high CO_2/CO partial pressure ratios (red and gray peaks, respectively, in Figure 5, panel a). In Figure 6 we report the positions of the spectroscopic lines identified in the C–O stretching SFG data as a function of the surface temperature (markers) in the 300–425 K range and as a function of the CO_2/CO partial pressure ratio in the gas feedstock. Dashed lines indicate average values. It can be observed that there is no overlap between the distinguished features, thus supporting the effectiveness of the spectral deconvolution.

Finally, focusing on the C–H stretching vibration region, we could detect contributions at 2850 ± 5 and 2935 ± 5 cm^{-1} (Figure 7). The signal-to-noise ratio is considerably worse than in the case of the C–O spectra due to several reasons. First of all, the dipole moment of C–H bonds is much lower with respect to the case of C–O bonds, thus yielding a consistently lower SFG signal. In addition, we remind that the SFG signal intensity is proportional to the square of the adsorbate surface density, at variance with other spectroscopic techniques where this dependence is linear, thus making the detection of low coverage species a challenge. Moreover, dipole effects can strongly influence intensities. Nevertheless, the presence of two distinct features separated by 85 ± 10 cm^{-1} is evident under different reaction conditions.

At this point of the discussion, a complete picture of the stable reaction intermediates requires a proper assignment of the detected spectroscopic features to known chemical species. Summarizing, three distinct C–O stretching modes (S_i, i = 1–3) have been observed in the SFG spectra besides the well-known contributions due to bridge and on-top CO on nickel. Moreover, two C 1*s* peaks appear under hydrogenation conditions in the NAP-XPS core level spectra, in addition to the features associated with atomic carbon, graphene domains, carbon monoxide, carbon dioxide, and carbonate. Two peaks

DOI: 10.1021/jacs.5b13366
J. Am. Chem. Soc. 2016, 138, 4146–4154

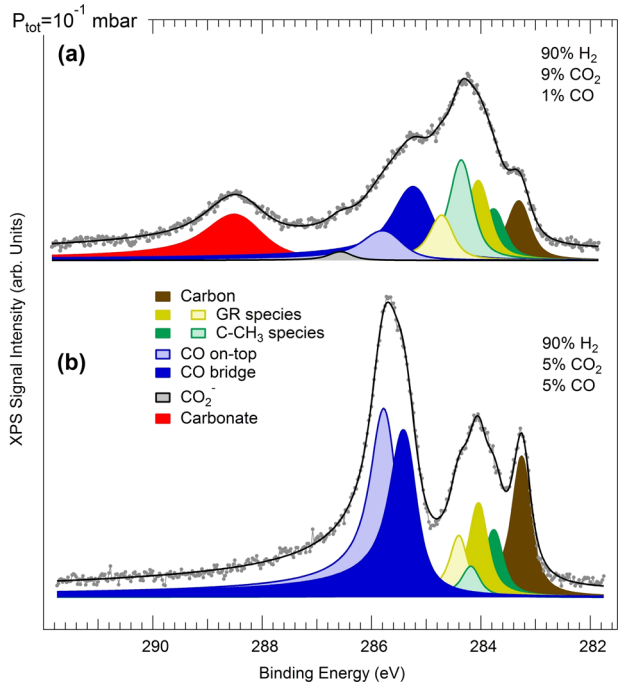

Figure 5. NAP-XPS C 1*s* core level spectra collected in situ during the reaction of CO, CO_2 and H_2 at a total pressure of 10^{-1} mbar on the Ni(110) surface at 425 K. Data sets corresponding to two different CO_2/CO pressure ratios are reported in the two panels (a and b). The deconvolution (color) of the data (gray dots) obtained by means of least-squares fitting (black curves) is also shown. [$h\nu$ = 450 eV].

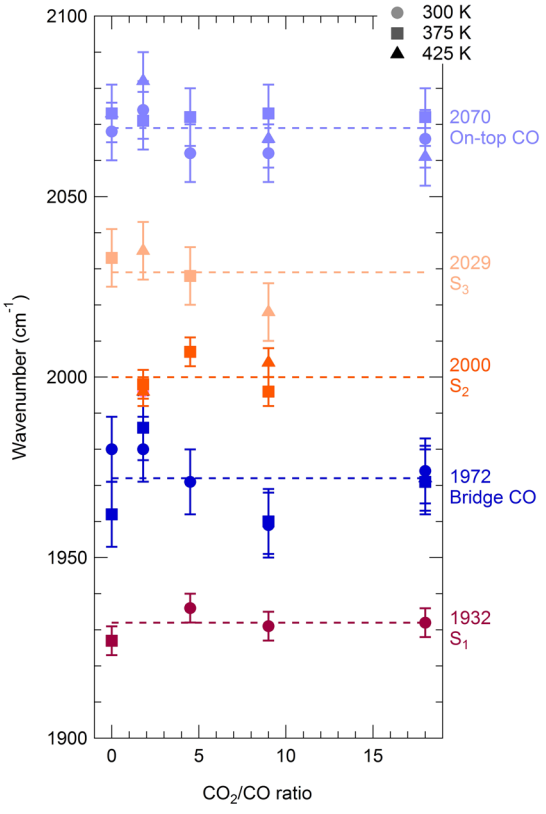

Figure 6. Position of the vibrational spectral features in the C−O region measured under reaction conditions in the 300−425 K temperature range as a function of the CO_2/CO partial pressure. Dashed lines indicate average values, shown on the right side.

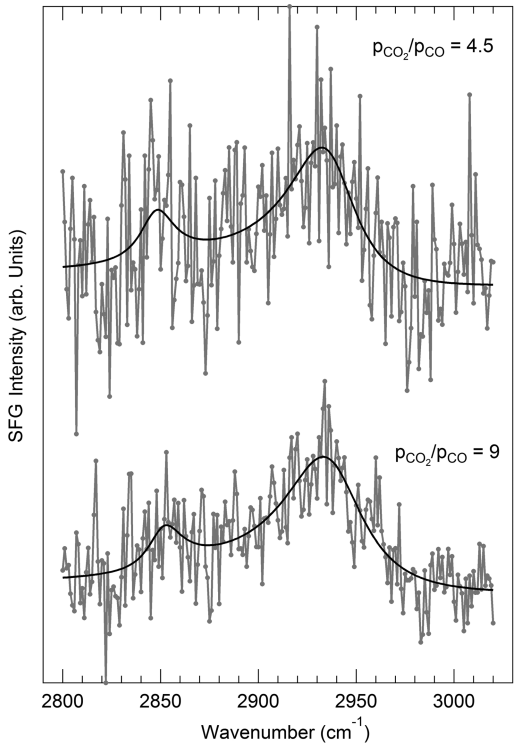

Figure 7. IR−vis SFG intensity spectra in the C−H stretching region collected in situ during the reaction of CO, CO_2 and H_2 at a total pressure of 10^{-1} mbar on the Ni(110) surface at 425 K for two different CO_2/CO pressure ratios (top and bottom). The best fit (black) of the data (gray) is shown. [λ_{vis} = 532 nm; p−p−p polarization].

show up also in the C−H stretching region of the vibrational data.

Starting from the lowest energy feature in the C−O stretching domain (S_1, 1927−1936 cm^{-1}), we propose to attribute it to CO species adsorbed in bridge configuration close to other species such as carbon and hydrogen atoms. Previous vibrational studies concerning thermal decomposition of formic acid on Ni(110) via a stable formate intermediate under UHV conditions report indeed coadsorption-induced vibrational splitting of the CO modes, yielding a contribution due to 2-fold carbon monoxide in the 1874−1940 cm^{-1} range.[45,46] Very interestingly, a recent theoretical report about the methanation reaction on nickel surfaces shows that the presence of hydrogen significantly reduces the CO activation barrier by causing a stretching of the CO bond as the CO-H complex forms. A stable reactive CO intermediate in the CO−H complex is proposed in the report, with a calculated C−O stretching energy of 1888 cm^{-1}.[7] In this framework COH is considered in chemical equilibrium with the CO−H coadsorption phase under methanation conditions. However, consistently with our results, the short-lived COH is not expected to be present on the surface in detectable amounts.

The remaining CO species (S_2, 1996−2007 cm^{-1}; S_3, 2018−2035 cm^{-1}) are instead associated with on-top configurations interacting with coadsorbed H and C phases, in agreement with previous infrared spectroscopy investigations under UHV conditions.[45,46] The observed shifts in the SFG spectra are ascribed to a combined effect related to lateral interactions between adsorbates. Coadsorption indeed changes the local environment, thus changing the chemical bonding of carbon

DOI: 10.1021/jacs.5b13366
J. Am. Chem. Soc. 2016, 138, 4146−4154

monoxide with the surface and the respective charge transfer, which reflects in a different C−O internal bond strength. In addition, dipole−dipole interactions due to coadsorption and local coverage effects can also induce shifts in the stretching frequencies.

Finally, the C 1*s* features at 283.7−284.0 eV and 284.1−284.6 eV, together with the vibrational fingerprints in the C−H stretching region, can be ascribed to a single, stable ethylidyne surface species (CCH_3). This tentative attribution is based on previous C 1*s* core level spectroscopic data available on the (111) terminations of Pt, Rh and Ir.[47−50] The reported splitting of about 0.4 eV between the peaks of the chemically nonequivalent C atoms in the molecule is mainly ascribed to their different interaction with the metallic substrate (coordination), rather than to the number of bonded hydrogen atoms.[47] Because of the crowding of our C 1*s* core level spectra arising from the concomitant presence at the surface of several chemical species, we are not able to determine the presence of associated vibrational splitting features of the methyl group as observed on Ir.[49] The observed variation of the intensity ratio of the two contributions (green) with reaction conditions is ascribed to coadsorption and local geometry effects, yielding core level shifts of the peak associated with the outer carbon atom of the ethylidyne molecule. It has indeed already been observed that the separation of the two ethylidyne peaks can reduce down to less than 0.2 eV upon coadsorption with CO,[50] thus overlapping in our case with the adjacent graphene contribution. These effects, in combination with possible and already reported strong photoelectron diffraction modulations of the signal,[50] in our case associated with changes in local adsorption geometries, can therefore further support our attribution. With reference to nickel surfaces, a stable ethylidyne intermediate was previously obtained from the reaction of ethylene, acetylene, and ethane with atomic hydrogen on Ni(111).[51] This CCH_3 species was characterized by means of electron energy loss spectroscopy under UHV conditions, yielding fingerprints of the C−H symmetric and antisymmetric stretching modes at 2883 and 2940 cm^{-1}, respectively, in rather good agreement with our observed values (2850 and 2935, respectively). Ethylidyne was defined as the most stable C_2 species on Ni(111) in the presence of coadsorbed hydrogen.[51] Interestingly, ab initio and molecular dynamics simulations of ethylene decomposition on Ni(111) again support the stability of ethylidyne, especially in the presence of coadsorbed hydrogen, as in the present case.[52] Remarkably, no evident fingerprints of a formate intermediate are observed, at variance with UHV low temperature experiments of CO_2 hydrogenation on Ni(110).[12,15] Indeed, in a previous study only a single vibrational C−H stretching component due to formate was observed at 2944 cm^{-1} on Ni(110).[12] Two vibrational features were instead observed for formate on Cu(110) at wavenumbers compatible with our SFG spectra: the C−H stretch was assigned to a contribution at 2849 cm^{-1}, while a peak at 2930 cm^{-1} was ascribed to the combination of the asymmetric COO stretch and of the CH deformation in Fermi resonance with the C−H stretch.[53] However, formate, obtained from the hydrogenation of carbon dioxide on Ni(110) as in the present case, contributes with a peak at 288.0 eV in the C 1*s* spectra,[12] which is not detected here (Figure 2, panel c) thus reasonably excluding this molecule as a candidate stable species. This evidence may indicate that a hydrogen-assisted CO_2 reduction and dissociation mechanism is more favored with respect to hydrogenation to formate, thus confirming previous data on Ni(110) under vacuum conditions where energy barriers of 0.12 and 0.30 eV where calculated for the two processes, respectively.[15] The opposite picture is instead found at copper surfaces, being the formation of a hydrocarboxyl intermediate energetically more costly.[54,55]

An overall picture of the complex reaction network developing at the Ni(110) surface can be derived, as depicted in Figure 8, on the basis of the experimental observations: (i)

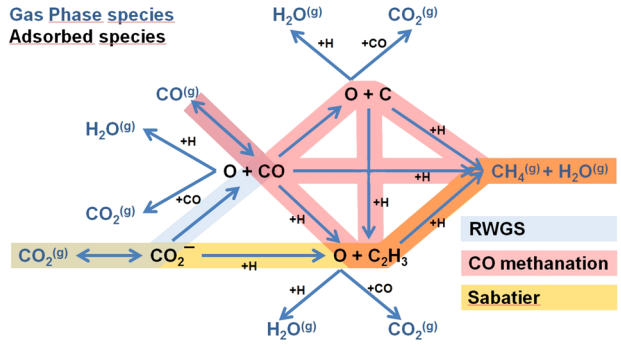

Figure 8. Qualitative scheme of the reaction network involving RWGS, carbon monoxide methanation, and carbon dioxide (Sabatier) methanation processes. Reaction stoichiometry is not considered for simplicity.

both carbon monoxide and dioxide can be hydrogenated; (ii) the methanation proceeds through stable surface species that have been identified, including metastable CO_2^-, atomic and graphenic C species, and possibly C_2H_3; (iii) CO_2 can both react with hydrogen (direct Sabatier process, yellow in Figure 8), or dissociate into CO and O (RWGS, cyan in Figure 8); (iv) CO, upon adsorption from the gas phase or stemming from the decomposition of carbon dioxide, can further decompose into atomic carbon and oxygen or undergo hydrogenation (CO methanation, pink in Figure 8) via a H−CO complex associated with the S_1 feature in the IR−vis SFG spectra; (v) atomic oxygen is removed from the nickel surface via fast reaction with carbon monoxide or by a much slower reaction pathway with hydrogen to produce water; (vi) stable species are adsorbed at the Ni surface since the graphene domes are inactive toward adsorption as known from the literature.[39,40]

In summary, the chemisorbed CO_2^- species at the Ni(110) surface plays a fundamental role both as a precursor in the RWGS mechanism and as a reactive species that undergoes fast conversion in the direct Sabatier methanation process. When adding hydrogen to the feedstock the two CO_2 conversion reactions are proposed to proceed through parallel routes. Since hydrogenation of CO is also effective, an alternative and parallel CO_2 methanation route involves RWGS, sequentially followed by the methanation of CO, an interesting insight that corroborates information on γ-alumina supported Ni catalysts.[3] Future isotope-labeling experiments may provide further details of the picture. Concerning the transferability of our results to applicative reaction conditions, both pressure and material gaps have to be considered. By exploiting the potential of NAP-XPS and SFG spectroscopy we extended to near-ambient pressure regimes the knowledge about this reaction previously obtained under vacuum conditions. Still, the role of the gas phase chemical potential may influence the actual phase of the metal surface (oxidic or carbidic) when further raising the pressure. With reference to the material gap, supported catalysts present

DOI: 10.1021/jacs.5b13366
J. Am. Chem. Soc. 2016, 138, 4146−4154

additional degrees of freedom. Therefore, finite-size effects of the metal nanoparticles, interaction with the support (e.g., alumina), charge and chemical spillover should be considered and investigated in detail.

CONCLUSIONS

The reduction of CO and CO_2 by H_2 on the Ni(110) single crystal surface has been investigated in situ at NAP conditions (10^{-1} mbar) by means of IR−vis SFG and NAP-XPS. Several stable surface species have been observed. In particular, in addition to atomic and graphenic C phases, five distinct CO species are detected, highlighting the role of coadsorption effects with H and C atoms, of H-induced activation of CO, and of surface reconstruction. The presence of stable carbonate has been demonstrated, originating from the interaction of gas phase CO_2 with atomic oxygen on the Ni surface due to the dissociation of CO_2 into CO + O. A metastable, activated CO_2^- species is also detected, being both a precursor to dissociation into CO and O (reverse water−gas shift mechanism) and a reactive species that undergoes conversion in the hydrogenation process (Sabatier methanation mechanism). We propose a tentative picture in which the two CO_2 conversion reactions proceed through parallel routes. In addition, since also hydrogenation of CO is effective, an alternative and parallel CO_2 methanation route involves RWGS, followed by the methanation of CO. Further kinetic investigations may be needed to definitely confirm this view, which is however in line with observations performed on Ni powder catalysts by means of chemical transient kinetics methods.[56] Finally, the stability of ethylidyne is proposed on the basis of our spectroscopic observations and comparison with previous literature.

ASSOCIATED CONTENT

Supporting Information

The Supporting Information is available free of charge on the ACS Publications website at DOI: 10.1021/jacs.5b13366.

O 1*s* core level spectra, their analysis and interpretation. (PDF)

AUTHOR INFORMATION

Corresponding Author

*vesselli@iom.cnr.it

Present Addresses

[§]Istitut für Materialchemie, Technische Universität Wien, Getreidemarkt 9/165, A-1060 Wien, Austria.

[∥]Zernike Institute for Advanced Materials, University of Groningen, Nijenborg 4, 9747AG Groningen, The Netherlands; School of Chemistry, University of Wollongong, Wollongong, Northfields Avenue, NSW, 2522, Australia.

Notes

The authors declare no competing financial interest.

ACKNOWLEDGMENTS

This research was supported by Italian MIUR through the project Futuro in Ricerca FIRB 2010 no. RBFR10J4H7. Consorzio per l'Incremento degli Studi e delle Ricerche dei Dipartimenti di Fisica dell'Università degli Studi di Trieste, Fondazione Casali, and Beneficentia Stiftung are also acknowledged for their contribution in the realization of the SFG setup. Part of the research leading to these results has received funding from the European Community's Seventh Framework Program (FP7/2007-2013) under Grant Agreement No. 226716. We acknowledge the Helmholtz-Zentrum Berlin for provision of synchrotron radiation beamtime at beamline ISISS of BESSY II.

REFERENCES

(1) Centi, G.; Perathoner, S. *Catal. Today* **2009**, *148*, 191−205.
(2) Wang, W.; Wang, S.; Ma, X.; Gong, J. *Chem. Soc. Rev.* **2011**, *40*, 3703−3727.
(3) Garbarino, G.; Riani, P.; Magistri, L.; Busca, G. *Int. J. Hydrogen Energy* **2014**, *39*, 11557−11565.
(4) Nerlov, J.; Sckerl, S.; Wambach, J.; Chorkendorff, I. *Appl. Catal., A* **2000**, *191*, 97−109.
(5) Nerlov, J.; Chorkendorff, I. *J. Catal.* **1999**, *181*, 271−279.
(6) Nerlov, J.; Chorkendorff, I. *Catal. Lett.* **1998**, *54*, 171−176.
(7) Andersson, M. P.; Abild-Pedersen, F.; Remediakis, I. N.; Bligaard, T.; Jones, G.; Engbæk, J.; Lytken, O.; Horch, S.; Nielsen, J. H.; Sehested, J. *J. Catal.* **2008**, *255*, 6−19.
(8) Remediakis, I. N.; Abild-Pedersen, F.; Nørskov, J. K. *J. Phys. Chem. B* **2004**, *108*, 14535−14540.
(9) Song, C. *Catal. Today* **2006**, *115*, 2−32.
(10) Freund, H.-J.; Roberts, M. W. *Surf. Sci. Rep.* **1996**, *25*, 225−273.
(11) Monachino, E.; Greiner, M.; Knop-Gericke, A.; Schlögl, R.; Dri, C.; Vesselli, E.; Comelli, G. *J. Phys. Chem. Lett.* **2014**, *5*, 1929−1934.
(12) Vesselli, E.; De Rogatis, L.; Ding, X.; Baraldi, A.; Savio, L.; Vattuone, L.; Rocca, M.; Fornasiero, P.; Peressi, M.; Baldereschi, A.; Rosei, R.; Comelli, G. *J. Am. Chem. Soc.* **2008**, *130*, 11417−11422.
(13) Ding, X.; De Rogatis, L.; Vesselli, E.; Baraldi, A.; Comelli, G.; Rosei, R.; Savio, L.; Vattuone, L.; Rocca, M.; Fornasiero, P.; Ancilotto, F.; Baldereschi, A.; Peressi, M. *Phys. Rev. B: Condens. Matter Mater. Phys.* **2007**, *76*, 195425.
(14) Dri, C.; Peronio, A.; Vesselli, E.; Africh, C.; Rizzi, M.; Baldereschi, A.; Peressi, M.; Comelli, G. *Phys. Rev. B: Condens. Matter Mater. Phys.* **2010**, *82*, 165403.
(15) Vesselli, E.; Rizzi, M.; De Rogatis, L.; Ding, X.; Baraldi, A.; Comelli, G.; Savio, L.; Vattuone, L.; Rocca, M.; Fornasiero, P.; Baldereschi, A.; Peressi, M. *J. Phys. Chem. Lett.* **2010**, *1*, 402−406.
(16) Peng, G.; Sibener, S. J.; Schatz, G. C.; Ceyer, S. T.; Mavrikakis, M. *J. Phys. Chem. C* **2012**, *116*, 3001−3006.
(17) Ferrin, P.; Mavrikakis, M. *J. Am. Chem. Soc.* **2009**, *131*, 14381−9.
(18) Peng, G.; Sibener, S. J.; Schatz, G. C.; Mavrikakis, M. *Surf. Sci.* **2012**, *606*, 1050−1055.
(19) Studt, F.; Abild-Pedersen, F.; Wu, Q.; Jensen, A. D.; Temel, B.; Grunwaldt, J. D.; Norskov, J. K. *J. Catal.* **2012**, *293*, 51−60.
(20) Rupprechter, G.; Weilach, C. *Nano Today* **2007**, *2*, 20−29.
(21) Rupprechter, G. *Catal. Today* **2007**, *126*, 3−17.
(22) Shen, Y. R. *Nature* **1989**, *337*, 519−525.
(23) Corva, M.; Feng, Z.; Dri, C.; Salvador, F.; Bertoch, P.; Comelli, G.; Vesselli, E. *Phys. Chem. Chem. Phys.* **2016**, *18*, 6763.
(24) Busson, B.; Tadjeddine, A. *J. Phys. Chem. C* **2009**, *113*, 21895−21902.
(25) Vidal, F.; Tadjeddine, A. *Rep. Prog. Phys.* **2005**, *68*, 1095−1127.
(26) Tian, C. S.; Shen, Y. R. *Surf. Sci. Rep.* **2014**, *69*, 105−131.
(27) Lambert, A. G.; Davies, P. B.; Neivandt, D. J. *Appl. Spectrosc. Rev.* **2005**, *40*, 103−145.
(28) Knop-Gericke, A.; Kleimenov, E.; Havecker, M.; Blume, R.; Teschner, D.; Zafeiratos, S.; Schlögl, R.; Bukhtiyarov, V.; Kaichev, V. V.; Prosvirin, I. P.; Nizovskii, A.; Bluhm, H.; Barinov, A.; Dudin, P.; Kiskinova, M. *Adv. Catal.* **2009**, *52*, 213−272.
(29) Shirley, D. *Phys. Rev. B* **1972**, *5*, 4709−4714.
(30) Doniach, S.; Sunjic, M. *J. Phys. C: Solid State Phys.* **1970**, *3*, 285−291.
(31) Bandy, B. J.; Chesters, M. A.; Hollins, P.; Pritchard, J.; Sheppard, N. *J. Mol. Struct.* **1982**, *80*, 203−208.
(32) Bauhofer, J.; Hock, M.; Küppers, J. *Surf. Sci.* **1987**, *191*, 395−405.
(33) Held, G.; Schuler, J.; Sklarek, W.; Steinrück, H. *Surf. Sci.* **1998**, *398*, 154−171.

DOI: 10.1021/jacs.5b13366
J. Am. Chem. Soc. 2016, 138, 4146−4154

(34) Katano, S.; Bandara, a; Kubota, J.; Onda, K.; Wada, a; Domen, K.; Hirose, C. *Surf. Sci.* **1999**, *427−428*, 337−342.
(35) Peters, K.; Walker, C.; Steadman, P.; Robach, O.; Isern, H.; Ferrer, S. *Phys. Rev. Lett.* **2001**, *86*, 5325−5328.
(36) Weatherup, R. S.; Amara, H.; Blume, R.; Dlubak, B.; Bayer, B. C.; Diarra, M.; Bahri, M.; Cabrero-Vilatela, A.; Caneva, S.; Kidambi, P. R.; Martin, M.-B.; Deranlot, C.; Seneor, P.; Schloegl, R.; Ducastelle, F.; Bichara, C.; Hofmann, S. *J. Am. Chem. Soc.* **2014**, *136*, 13698−13708.
(37) Patera, L. L.; Africh, C.; Weatherup, R. S.; Blume, R.; Bhardwaj, S.; Castellarin-Cudia, C.; Knop-Gericke, A.; Schloegl, R.; Comelli, G.; Hofmann, S.; Cepek, C. *ACS Nano* **2013**, *7*, 7901−7912.
(38) Patera, L. L.; Bianchini, F.; Troiano, G.; Dri, C.; Cepek, C.; Peressi, M.; Africh, C.; Comelli, G. *Nano Lett.* **2015**, *15*, 56−62.
(39) Grånäs, E.; Knudsen, J.; Schröder, U. a.; Gerber, T.; Busse, C.; Arman, M. a.; Schulte, K.; Andersen, J. N.; Michely, T. *ACS Nano* **2012**, *6*, 9951−9963.
(40) Grånäs, E.; Andersen, M.; Arman, M. A.; Gerber, T.; Hammer, B.; Schnadt, J.; Andersen, J. N.; Michely, T.; Knudsen, J. *J. Phys. Chem. C* **2013**, *117*, 16438−16447.
(41) Wei, M.; Fu, Q.; Yang, Y.; Wei, W.; Crumlin, E.; Bluhm, H.; Bao, X. *J. Phys. Chem. C* **2015**, *119*, 13590−13597.
(42) Vesselli, E.; De Rogatis, L.; Baraldi, A.; Comelli, G.; Graziani, M.; Rosei, R. *J. Chem. Phys.* **2005**, *122*, 144710.
(43) Meyer, G.; Reinhart, E.; Borgmann, D.; Wedler, G. *Surf. Sci.* **1994**, *320*, 110−122.
(44) Seyller, T.; Borgmann, D.; Wedler, G. *Surf. Sci.* **1998**, *400*, 63−79.
(45) Haq, S.; Love, J. G.; Sanders, H. E.; King, D. A. *Surf. Sci.* **1995**, *325*, 230−242.
(46) Haq, S.; Love, J. G.; King, D. A. *Surf. Sci.* **1992**, *275*, 170−184.
(47) Papp, C.; Steinrück, H.-P. *Surf. Sci. Rep.* **2013**, *68*, 446−487.
(48) Lorenz, M. P. a; Fuhrmann, T.; Streber, R.; Bayer, a; Bebensee, F.; Gotterbarm, K.; Kinne, M.; Tränkenschuh, B.; Zhu, J. F.; Papp, C.; Denecke, R.; Steinrück, H.-P. *J. Chem. Phys.* **2010**, *133*, 014706.
(49) Lizzit, S.; Baraldi, A. *Catal. Today* **2010**, *154*, 68−74.
(50) Wiklund, M.; Beutler, A.; Nyholm, R.; Andersen, J. *Surf. Sci.* **2000**, *461*, 107−117.
(51) Bürgi, T.; Trautman, T. R.; Gostein, M.; Lahr, D. L.; Haug, K. L.; Ceyer, S. T. *Surf. Sci.* **2002**, *501*, 49−73.
(52) Arifin, R.; Shibuta, Y.; Shimamura, K.; Shimojo, F.; Yamaguchi, S. *J. Phys. Chem. C* **2015**, *119*, 3210−3216.
(53) Bowker, M.; Haq, S.; Holroyd, R.; Parlett, P. M.; Poulston, S.; Richardson, N. *J. Chem. Soc., Faraday Trans.* **1996**, *92*, 4683.
(54) Gokhale, A. A.; Dumesic, J. A.; Mavrikakis, M. *J. Am. Chem. Soc.* **2008**, *130*, 1402−1414.
(55) Grabow, L. C.; Mavrikakis, M. *ACS Catal.* **2011**, *1*, 365−384.
(56) Vesselli, E.; Schweicher, J.; Bundhoo, A.; Frennet, A.; Kruse, N. *J. Phys. Chem. C* **2011**, *115*, 1255−1260.
(57) Weatherup, R. S.; Bayer, B. C.; Blume, R.; Ducati, C.; Baehtz, C.; Schlögl, R.; Hofmann, S. *Nano Lett.* **2011**, *11*, 4154−4160.
(58) Grüneis, A.; Kummer, K.; Vyalikh, D. V. *New J. Phys.* **2009**, *11*, 073050.
(59) Benayad, A.; Li, X. *J. Phys. Chem. C* **2013**, *117*, 4727−4733.

DOI: 10.1021/jacs.5b13366
J. Am. Chem. Soc. 2016, 138, 4146−4154